Available online at www.sciencedirect.com

SCIENCE DIRECT®

Journal of Volcanology and Geothermal Research 135 (2004) 147–168

Journal of volcanology and geothermal research

www.elsevier.com/locate/jvolgeores

The evolution of an active silicic lava flow field: an ETM+ perspective

Andrew J.L. Harris[a,*], Luke P. Flynn[a], Otoniel Matias[b], William I. Rose[c], Julio Cornejo[d]

[a] *HIGP/SOEST, University of Hawai'i, 2525 Correa Road, Honolulu, HI 96822, USA*
[b] *INSIVUMEH, 7a Av. 14-57, Zona 13, Guatemala City, Guatemala*
[c] *Department of Geological Engineering, Geology and Geophysics, Michigan Technological University, Houghton, MI 49931, USA*
[d] *Santa Maria Volcano Observatory, c/o INSIVUMEH, 7a Av. 14-57, Zona 13, Guatemala City, Guatemala*

Accepted 5 December 2003

Abstract

An active dacitic lava flow began advancing down the south flank of the Caliente dome unit (Santiaguito Volcano, Guatemala) during July 1999. By January 2002 continued activity had built a ~ 1-km^2, 66 × 10^6 m^3 flow field. Using a time series of Landsat 7 ETM+ images and field observations the evolution and characteristics of this flow field are described. Throughout the period of emplacement, flow front advance rates have been extremely slow (2–13 m day^{-1}), consistent with a viscosity of 10^9–10^{10} Pa s. However, extremely efficient thermal insulation has allowed flow fronts to extend up to 3.75 km from the vent, in spite of extrusion rates of just 0.5–1.6 m^3 s^{-1}. Surface temperatures along most of the flow are less than 75 °C, and typically ~ 40 °C. Such surface temperatures result in extremely low rates of heat loss, and thus core cooling of just 0.03–0.09 °C h^{-1} or 0.01–0.12 °C m^{-1}. The flow field itself clearly displays the same systematic, spatial variations in structure and morphology as described by Lipman and Banks [Prof. Pap. - Geol. Surv. U. S. 1350 (1987) 1527] for a basaltic 'a'a flow, where a stable, and then transitional, channel zone feeds a distal area of dispersed flow. The stable channel dominates the proximal and medial sections of the flow field, and comprises a 90–375-m-wide channel flanked by levees that are up to 117 m high. A marked increase in the flow area and thickness occurred between January 2001 and January 2002, and was coincident with an increase in the extrusion rate from 0.5–0.7 to 1.2–1.6 m^3 s^{-1}. However, this increase in extrusion rate did not bring an increase in flow lengths, indicating that the flow may have reached its cooling-limited length around January 2001.

Keywords: ETM+; dacite; block lava flow; rheology; Santiaguito

1. Introduction

Extrusion of dacitic lava has persisted at Santiaguito since 1922 (Rose, 1987). By 2000, persistent extrusion at a time-averaged rate of ~ 0.45 m^3 s^{-1} had built a 1.1-km^3 complex of dome and block lava flow units. Although persistent, extrusion rates have showed marked cyclicity in which spurts of extrusion at 0.6–2.1 m^3 s^{-1} lasting 3–6 years have been punctuated by 4–11-year-long periods of lower (~ 0.2 m^3 s^{-1}) extrusion rate (Rose, 1972, 1987; Harris et al., 2003). Since 1958, activity

* Corresponding author. Tel.: +1-808-956-3157; fax: +1-808-956-6322.
E-mail address: Harris@higp.hawaii.edu (A.J.L. Harris).

0377-0273/$ - see front matter © 2004 Elsevier B.V. All rights reserved.
doi:10.1016/j.jvolgeores.2003.12.011

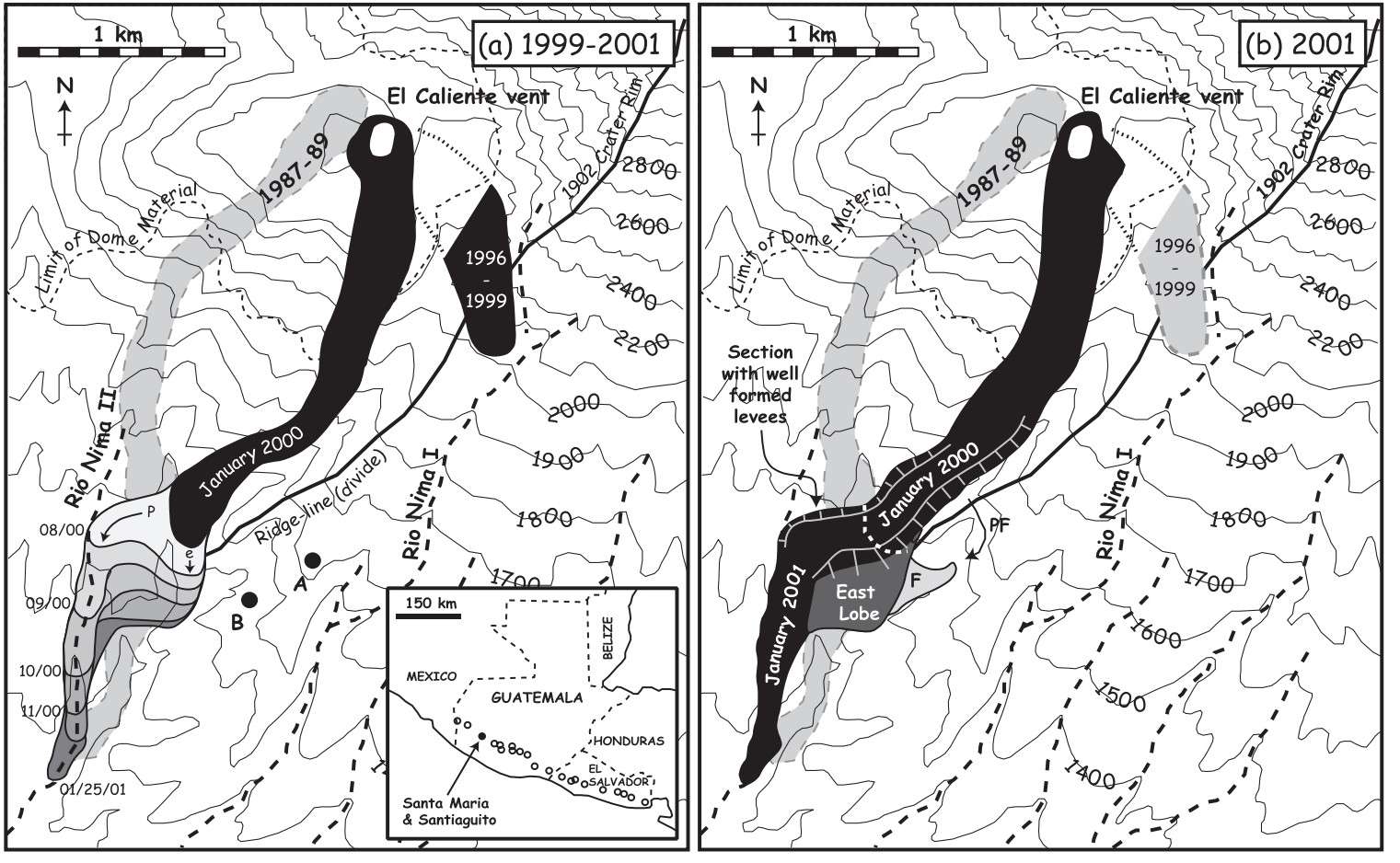

Fig. 1. (a) Map showing advance of the block lava flow at Santiaguito during January 2000 and 2001, along with flow field emplaced during 1987–1989 and 1996–1999. Extents of the flow during January 2000 and 2001 are mapped using ETM+ images. Flow front positions during August–December 2000 are located from ground-based mapping. Arrows marked P and e show the primary and secondary axes of advance during January–December, 2000. Locations marked A and B locate our field observation sites for the proximal and medial flow sections, respectively. (b) Block flow area mapped using the January 2001 ETM+ image. The unit emplaced along the eastern margin of the lower-medial section during January–December 2000 is marked as the East lobe. Path of rock falls into the adjacent valley due to the east levee overtopping the valley crest is marked PF, and subsequent valley fill is denoted with an F. Also mapped is the location of the ETM+ located January 2000 flow front and the channelized section.

during high extrusion rate phases has been dominated by block lava flow emplacement, where high extrusion rate phases during 1958–1972, 1972–1986 and 1986–1996 led to the emplacement of block lava flows 2.3, 2.1 and 3.6 km in length, respectively (Harris et al., 2003). An 8th cycle began during 1996. As with the previous three cycles, the opening phase of high extrusion rate activity has resulted in the emplacement of block lava flow units. The first unit in this cycle was active during 1996–1999. This flow advanced down the SE flank of the Caliente vent, breached the 1902 explosion crater rim and came to a halt in the headwaters of the Rio Nima I (Fig. 1). Beginning in mid-July 1999 a second active block flow began to advance down the southern flank of the Caliente (Fig. 1). This block flow remained active through January 2002. It is the emplacement history of this second flow unit that will be the focus of this paper.

The emplacement of the 1999–2002 block lava flow has presented an excellent opportunity to observe and measure the evolution of an active silicic lava flow. Our initial observations of this flow unit were published in Harris et al. (2002) and focused on the first 7 months of flow emplacement. Our analysis focused on an examination of a Landsat 7 Enhanced Thematic Mapper Plus (ETM+) image acquired on January 23, 2000 and data acquired during field work simultaneous with the image acquisition. This analysis allowed us to define the main emplacement and rheological features that characterized the opening phase of flow emplacement.

Since January 2000, extrusion has continued for another 24 months, such that the flow field has evolved significantly and a number of new features have developed, including the development of a well-formed master channel. Here our aim is to update Harris et al. (2002) and provide a full chronology of the morphological and rheological evolution of this silicic lava flow. To achieve this we have acquired two further ETM+ images during 2001–2002 and completed another two field campaigns synchronous with each ETM+ overpass. Thus, in completing our chronology, we also illustrate how ETM+ data can be used to track, measure and map an evolving lava flow field.

2. ETM+ and field data

A review of the use of ETM+ and its capabilities, with special reference to the identification of volcanic thermal features, is given in Flynn et al. (2001). Here we use three ETM+ images acquired on January 23, 2000, January 25, 2001 and January 19, 2002 to contribute to a chronology of the 1999–2002 block flow emplacement at Santiaguito. Mainly we use the 30-m-pixel short-wave infrared bands (bands 7 and 5), the 60-m thermal infrared band (band 6) and the 15-m panchromatic (visible) band (band 8) to gain two sets of parameters: dimensional and thermal (Fig. 2).

To gain the dimensional parameters for this lava flow we use the 15-m spatial resolution data from the ETM+ panchromatic band (band 8). We use these data to map the flow and to extract flow dimensions, namely flow length and width. We are also able to obtain flow thickness to an accuracy of 1 pixel (15 m) from these data, where outer levee heights (H_L) are obtained from shadows apparent in the band 8 data to the west of the flow unit. Here:

$$H_L = L_s \tan(\alpha) \quad (1)$$

in which L_s is the shadow length, measured along a line parallel to the sun azimuth, and α is the sun elevation. In addition, shadows cast by the levee inner banks allow us to obtain the level of the flow within the channel. Using this method, flow profiles were constrained every 45 m down flow, i.e. for every third pixel. By integrating the cross-sectional lava area under and between each profile we are able to calculate flow volume.

To extract the thermal parameters we applied the methodologies laid out in Harris et al. (2002, 2003). These use data from the ETM+ thermal band (band 6) and two short wave infrared bands (bands 5 and 7) to estimate flow surface temperature, heat loss, crust thickness, extrusion rates and cooling rates. Rather than repeat these methodologies here, we summarize them in Appendix A.

Field work was also carried out during January 2000, 2001 and 2002 synchronous (or near-synchronous) with each Landsat 7 overpass. During these field campaigns, thermal and dimensional measurements were made from a distance of 250–1000 m

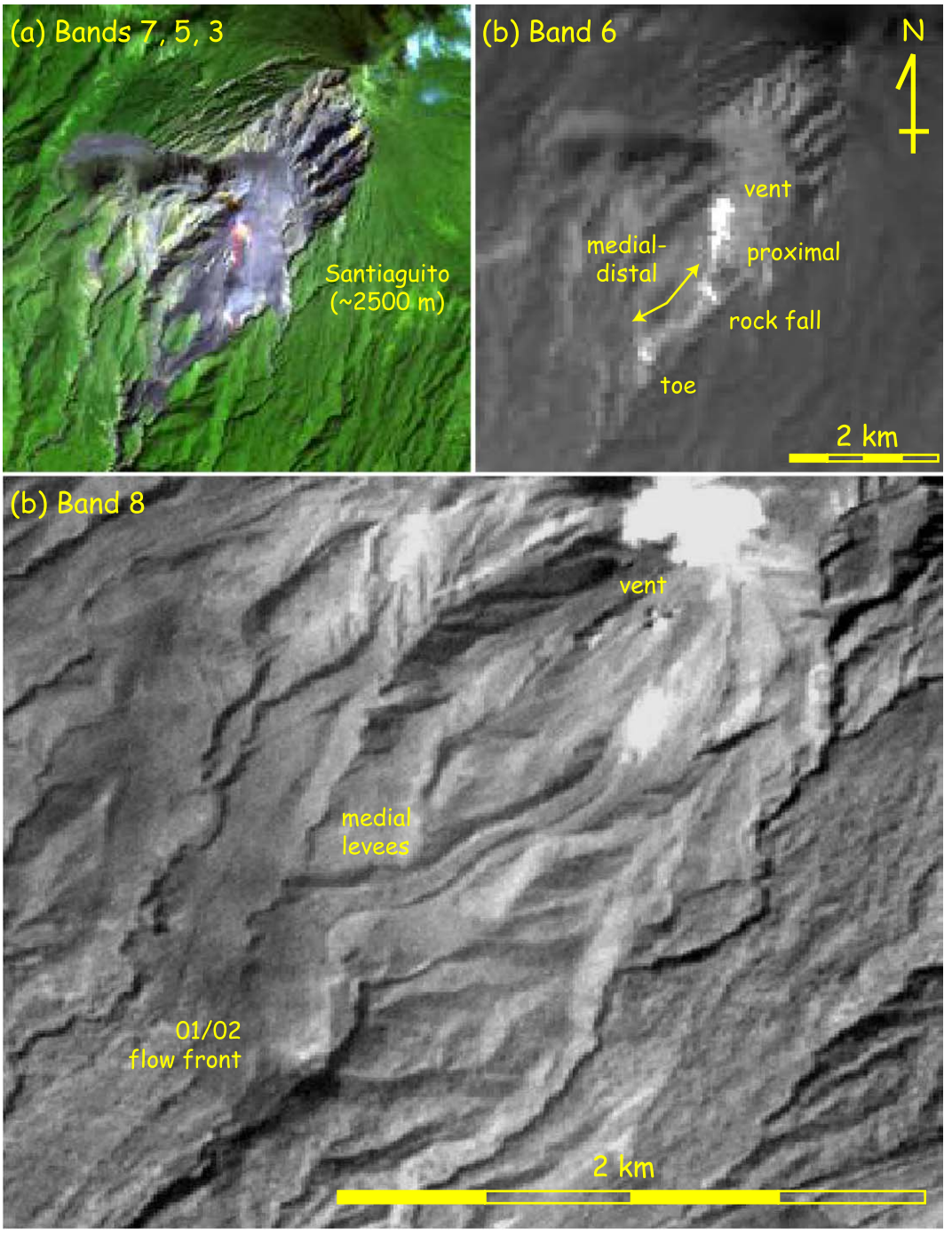

Fig. 2. (a) January 2000 band 7 (2.09–2.35 μm), 5 (1.55–1.75 μm), 3 (0.63–0.69 μm) ETM+ image, showing a thermal anomaly (yellow-orange colors) only at the vent and flow toe. (b) January 2000 band 6 (10.4–12.5 μm) ETM+ image of the same area showing a thermal anomaly down the entire length of the active lava flow (lighter tones = higher temperatures). (c) January 2001 band 8 (0.52–0.90 μm) ETM+ image of the active lava flow at Santiaguito. Shadows cast by the levees of the flow are readily apparent across the flow medial section.

using a thermal infrared thermometer and a laser range finder (see Fig. 1 for ground-based observation sites). These measurements were made from the ground and from helicopter over-flights. An over-flight was made during each of the three field campaigns. In all cases the active flow surface filled the 1° infrared thermometer field of view. Slides and video obtained during these over-flights were also used to aid in mapping the flow dimensions.

3. Flow field evolution: chronology, dimensions and morphology

We begin by describing the evolution of the flow field during the first 2.5 years of emplacement (July 1999–January 2002). As stated above, our description and measurements are based mostly on observations from three ETM+ acquisitions and field campaigns made in January of each year. Our descriptions are,

Table 1
ETM+ derived flow dimensions

Date	January 23, 2000	January 25, 2001	January 19, 2002
Flow length (km)	2.4	3.85	3.75
West levee height			
Minimum (m)	15	15	29
Maximum (m)	88	73	117
Mean (m)	42	35	66
Standard deviation (m)	22	19	24
West levee width			
Minimum (m)	15	15	30
Maximum (m)	90	75	120
Mean (m)	41	36	68
Standard deviation (m)	22	20	25
Channel width			
Minimum (m)	45	45	90
Maximum (m)	150	195	375
Mean (m)	103	129	182
Standard deviation (m)	24	37	85
East levee width			
Minimum (m)	15	15	15
Maximum (m)	60	105	90
Mean (m)	35	45	60
Standard deviation (m)	10	28	20
Flow width			
Minimum (m)	105	75	210
Maximum (m)	240	330	495
Mean (m)	179	209	310
Standard deviation (m)	33	67	74
Channel level[a]			
Minimum (m)	0	0	0
Maximum (m)	0	29	59
Mean (m)	0	10	23
Standard deviation (m)	0	11	16
Number of profiles	25	50	50

[a] Level, below levee rim, of the channel-contained flow surface.

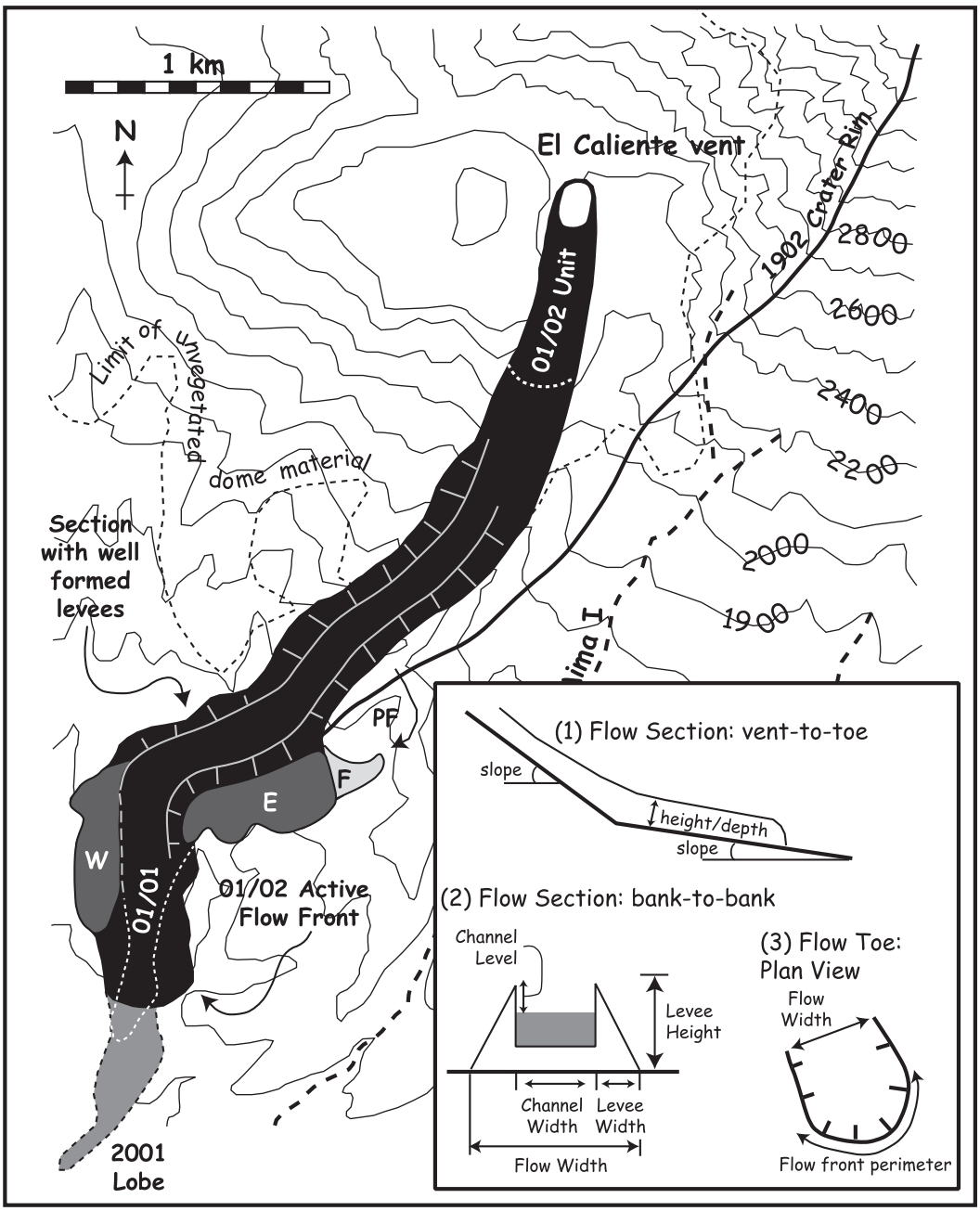

Fig. 3. Block flow area mapped using the January 2002 ETM+ image. The East lobe emplaced during 2000 is marked E, and units emplaced along the western margin of the lower-medial section during January–December 2001 are marked W. Also mapped is: (i) The inactive, frontal unit emplaced during January–December 2001, the flow front location mapped in January 2001. (ii) The January 19, 2002 flow front location of the upper unit that began advancing on December 29, 2000. (iii) The location of continued rock falls from the east levee (PF) and valley fill (F).

however, supplemented by observations made throughout the year from the Santa Maria Volcano Observatory. A summary of the dimensional evolution of the block flow obtained from the ETM+ images is given in Table 1, and maps summarizing the flow field evolution are given in Figs. 1–3. Fig. 3 also includes a schematic showing the main flow dimensional parameters measured and used in this study.

3.1. July 1999–December 2000

The 1999–2002 block flow began moving away from the El Caliente vent around July 14, 1999 (Harris et al., 2002). By the time of our first ETM+ image (January 23, 2000) and field campaign (January 21–23, 2000), the flow front had extended 2.4 km from the vent (Fig. 1a). Over the first kilometer of its length, the flow descended the steep (~ 30°) flanks of the Caliente dome unit. Over this proximal section the flow was relatively narrow and thin, with an ETM+ derived width and thickness of ~ 105 and ~ 15 m, respectively. At the break of slope that marks the dome base slopes fall to 22–27°. Around this point, the flow thickened considerably with the outer levees reaching 88 m in height (Fig. 4). The increase in thickness was matched by an increase in flow width to 150–240 m (Fig. 5).

The flow front was 18–30 m high, 165 m wide and had a perimeter of 200 m. During our January 2000

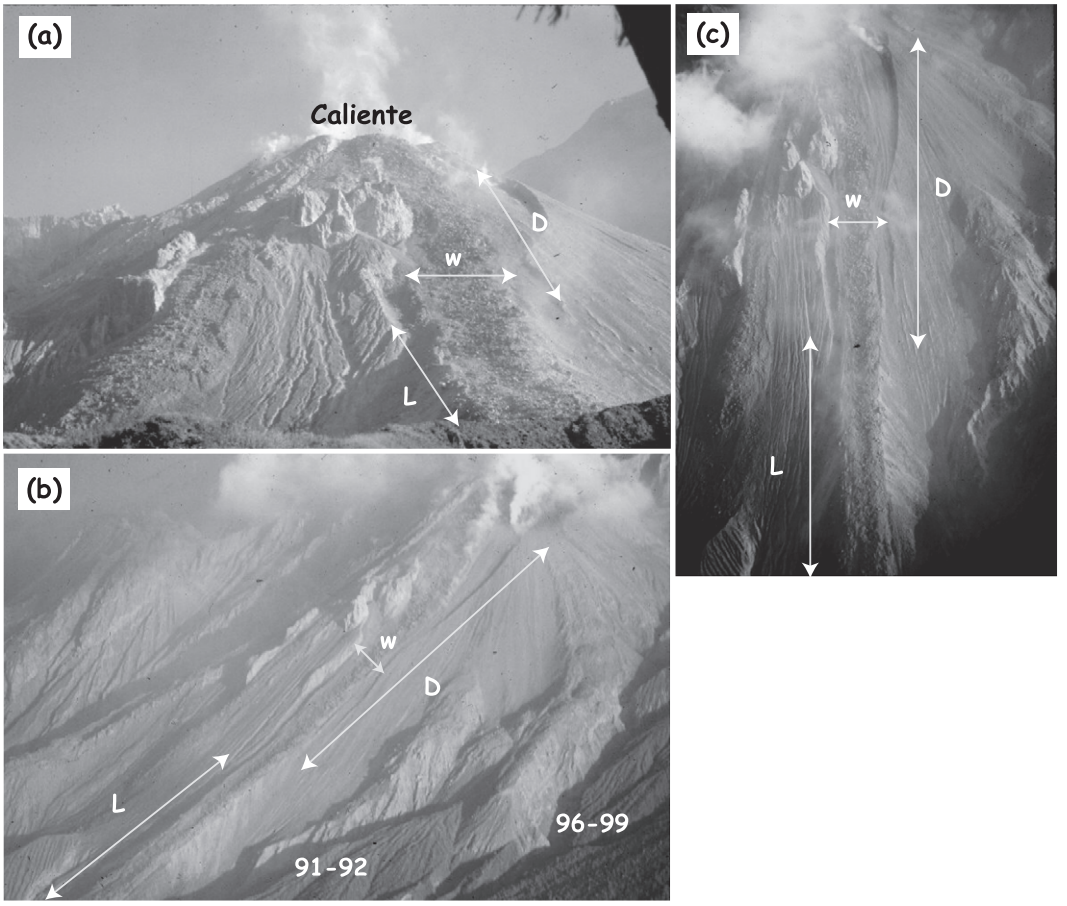

Fig. 4. Three views of the distal and upper-medial section of the block flow during January 2000. Views are (a) looking NNE (from observation site A, Fig. 1), (b) aerial oblique looking west (also showing flow unit emplaced during 1991–1992 and 1996–1999), and (c) aerial, vertical. In each case the same dimensions are marked w, D and L. Width w identifies the flow width at the distal section and is ~ 105 m across. Length D identifies the first kilometer of the flow showing no outer levees (flow is ~ 15 thick). Length L identifies a ~ 750-m-long segment of the upper medial section showing high outer levees forming where the flow moves off of the dome flank (outer levees are 59–88 m high).

field observations we noted two axes of advance: a primary axis roughly central to the flow front, and a secondary axis at the eastern margin (Harris et al., 2002). Flow front locations fixed by daily-to-weekly visual observations between August and December 2000 revealed that advance remained centered on these two axes (Fig. 1a). The central axis entered the headwaters of the Rio Nima II and extended a further 1.25 km down a narrow, steep-sided ravine to reach 3.65 km from the vent by the end of December 2000. The eastern lobe, however, became ponded in a topographic basin such that its rate of advance was lower and spread

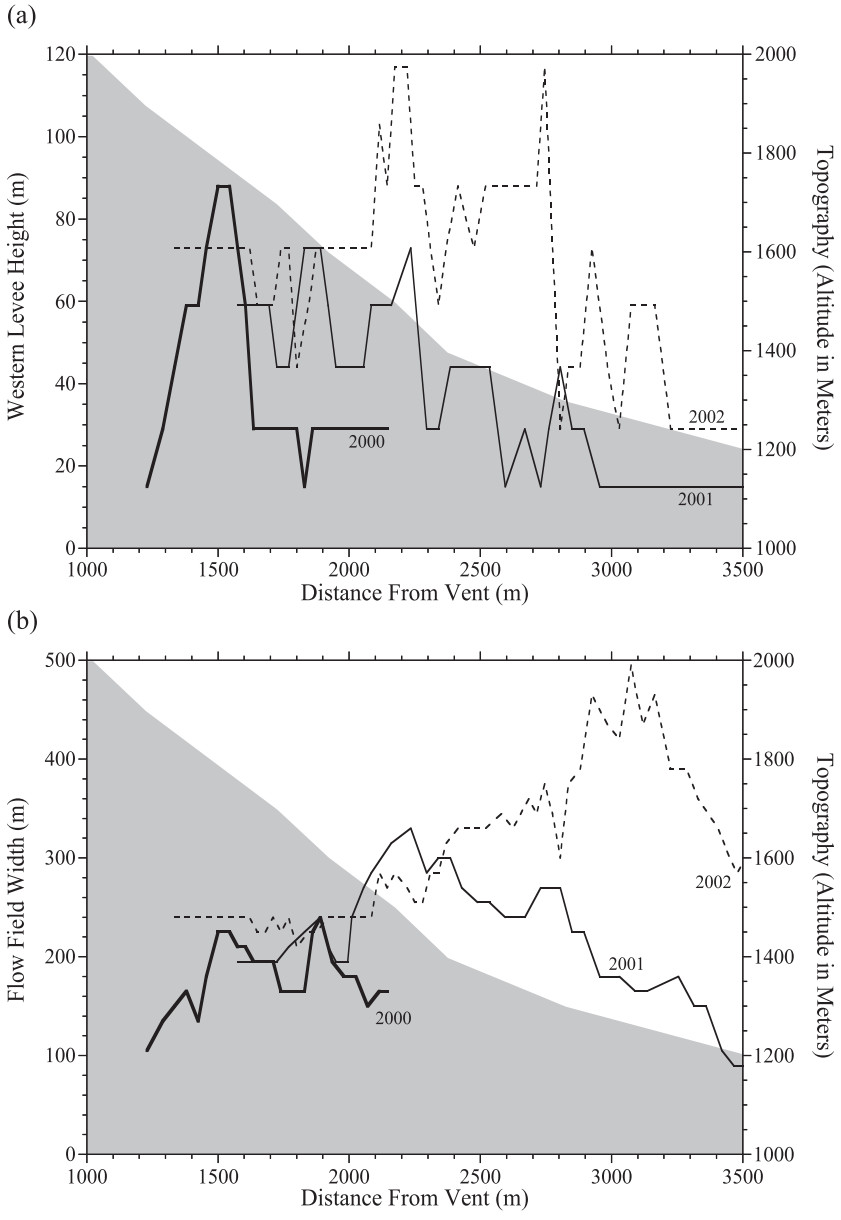

Fig. 5. ETM+ derived down-flow variation in (a) western levee height and (b) flow field width. In each case, topography is given by the gray shaded area.

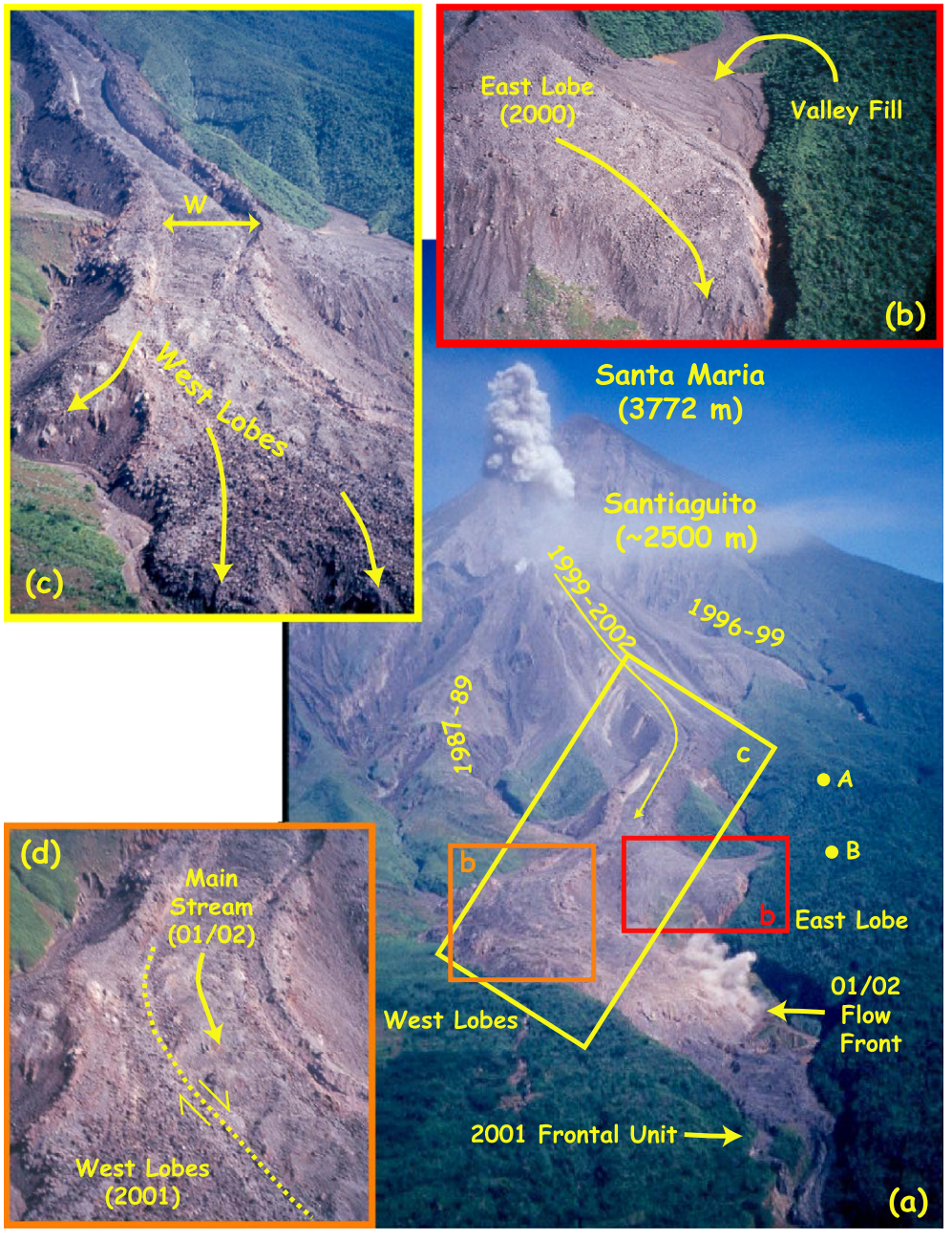

Fig. 6. (a) Oblique aerial photograph of 1999–2002 block lava flow field. Field observation sites A and B are indicated, along with the coverage of inset figures (b), (c) and (d) (given by the color coded boxes). For scale, distance from vent to 01/02 flow front is 3.75 km. View is to the NNE. (b) Oblique aerial view of the East Lobe (emplaced during 2000), picture is ~ 600 m across. View is North and shows valley fill due to deposition of flow-derived debris during 2000–2002 and east lobe flow front. (c) Oblique aerial view of the west lobes (emplaced during 2001) and medial channel section, channel is ~ 150 m wide at w, view is NE (d) Oblique aerial view of the west lobes and shear zone that delimits the lower-medial channel section. Main stream is ~ 200 m wide, view is ENE. All pictures are from a 01/19/02 over flight.

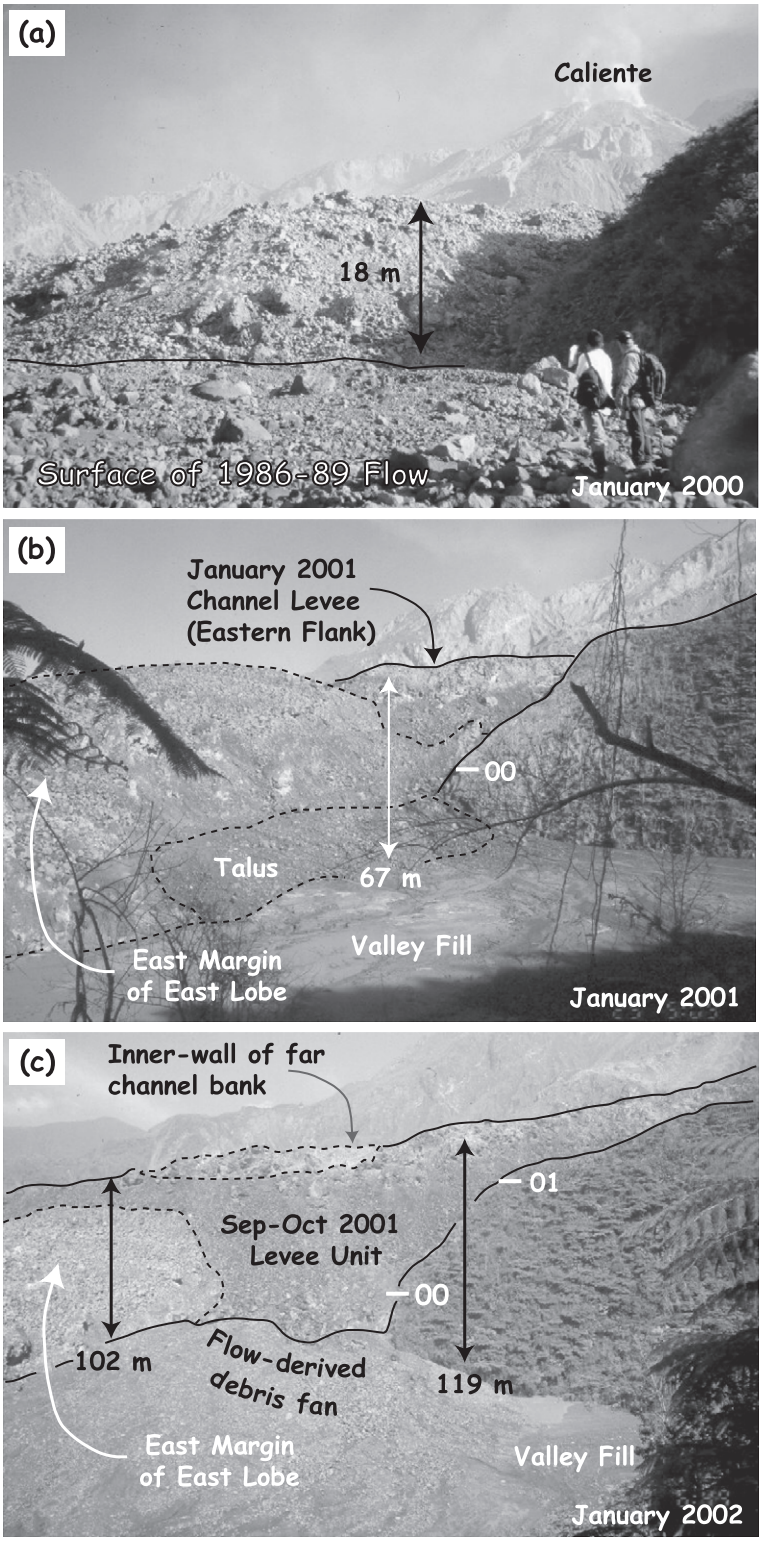
(a)
Caliente
18 m
Surface of 1986-89 Flow
January 2000
(b)
January 2001
Channel Levee
(Eastern Flank)
00
Talus
67 m
Valley Fill
East Margin
of East Lobe
January 2001
(c)
Inner-wall of far
channel bank
01
Sep-Oct 2001
Levee Unit
00
102 m
Flow-derived
debris fan
119 m
East Margin
of East Lobe
Valley Fill
January 2002

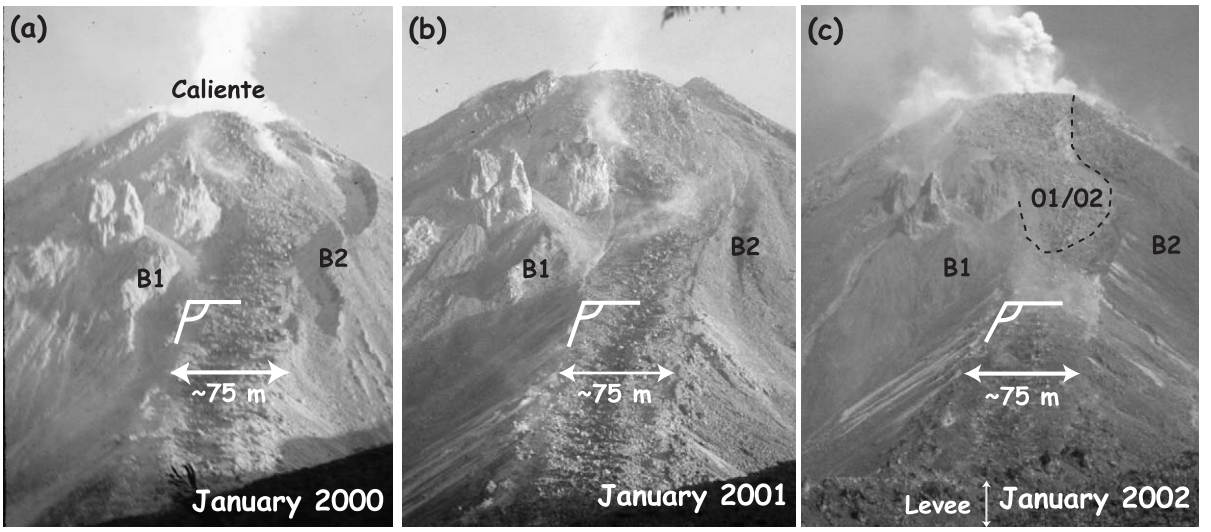

Fig. 8. Year-on-year comparison of the proximal flow section from field observation site A (Figs. 1 and 6). (a) January 2000, (b) January 2001, and (c) January 2002, view is NNE. The main stream width remains approximately constant, but thickening of the flow and broadening of the levees causes: (1) gradual burial of scarps at B1 and B2, (2) decrease in the slope of the flow surface, and (3) the levee crest to rise above the ridge in the foreground.

over a broader front. This unit contributed to a broad eastern-marginal lobe that added to the width of the flow field along the lower-medial section (Fig. 1a).

3.2. January 2001

Our next ground-based observations were made during January 25–28, 2001, simultaneous with an ETM+ acquisition on January 25. A helicopter overflight on January 27 revealed that the primary axis of advance remained confined within the narrow canyon of the Nima II. The ETM+ image revealed that this arm of the flow had extended 3.85 km from the vent and had a ~ 75 m wide flow front (Fig. 1b). The narrow width of the flow over the distal 500 m (Fig. 5) can be explained by entrapment in the Nima II canyon. The broad eastern lobe had stagnated, its supply cut off by the development of a well-formed levee along the medial section of the flow (Figs. 1b and 6). The emplacement of this unit on the eastern margin of the flow contributed to a 225–330 m wide bulge in the lower-medial section (Fig. 1b), compared with a flow field width of 195–240 m above this location and 75–180 m below it (Fig. 5).

Over the first 2 km of the flow, the width was similar to that measured in January 2000 (Fig. 5). However, the height of the outer levees had increased significantly (Fig. 7). At the location of the January 2000 flow front (~ 2.4 km from the vent) where levee heights had formerly been 18–30 m, ETM+ derived heights for the western levee were 15–73 m by January 2001 (Fig. 5). This is in good agreement with heights of ~ 67 m obtained for the eastern levee using a laser range finder along this section.

The flow advanced ~ 0.65 km further during 2001, before stalling at a maximum distance of 4.5 km from the vent (Fig. 3).

3.3. January 2002

Our next set of observations from the ground and air were made during January 9–11, 2002, with an

Fig. 7. Year-on-year comparison of the medial flow section from field observation site B (Figs. 1 and 6). (a) January 2000: 18 m high flow front advancing over the surface of the 1986–1989 flow unit. View is North. (b) January 2001: Outer-flank of the of east lobe and channel levee outer bank. View is East, tick marked 00 locates approximate flow surface in January 2000. (c) January 2002: Outer-flank of the of east lobe and channel levee outer bank showing levee development. View is East, ticks marked 00 and 01 locate approximate flow surface in January 2000 and levee rim in January 2001, respectively.

ETM+ overpass following on January 19. Helicopter-based observations revealed that the active flow front was extending over the stalled and inactive 2001 flow toe (Fig. 6). In addition, a new unit was advancing over the proximal section of the flow, apparent as a tongue of lighter toned material extending from the vent (Fig. 8). This new unit began moving away from the vent around December 28, 2001, and followed a significant collapse event from the vent region that generated a 500 m long pyroclastic flow down the SE flank of the Caliente. The ETM+ image revealed that, while the main flow front was 29 ± 3 m high, 225 m wide and 3.75 km from the Caliente vent, the new flow front was ~ 60 m wide and had advanced $\sim 700 \pm 60$ m from the vent (Fig. 3).

Between January 2001 and 2002, the flow continued to increase in thickness. Along the medial section flow levees gained in height considerably, attaining a maximum height of 117 m (Fig. 5; Table 1). At our field observation site B, ~ 2.4 km from the vent, west levee heights had increased to 59–88 m (ETM+ derived) and east levee heights were 100–120 m (laser range-finder derived). Much of this height increase was due to construction of a compound levee, where new lava had been plastered to the levee tops and tumbled down the outer flanks during a lava pulse that moved down the channel in September–October 2001. This new levee unit was apparent as a darker unit with smaller blocks than the underlying unit and contained many oxidized, massive outcrops. In contrast, the underlying, older levee unit was lighter toned and composed of larger blocks (Fig. 7).

A good gauge for the increase in levee height over this medial section is provided by the ridge line that is responsible for the change in flow direction from SSW down the dome flank to SW across the medial section

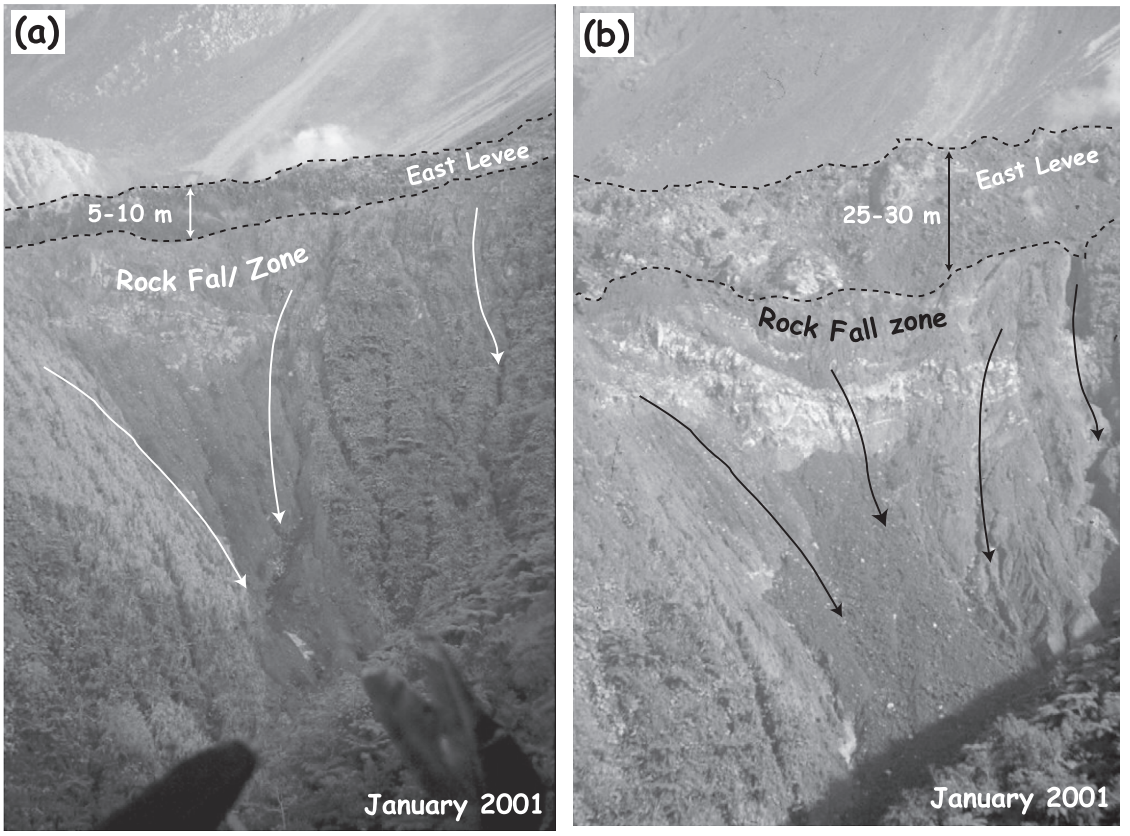

Fig. 9. Year-on-year comparison of the eastern levee and zone of rock fall into adjacent valley: (a) January 2001, and (b) January 2002. View is north from field observation site A (Figs. 1 and 6).

(Fig. 1a). In January 2000 the levee crest was below this ridge line. By January 2001, however, the levee crest was 5–10 m above the ridge line, and was 25–30 m above the ridge line by January 2002 (Fig. 9). Rock falls from the levee outer flank into the adjacent valley had three effects. First, they cut an increasingly large vegetation-free swath down the valley-side (Fig. 9). Second, the passage of rock-fall generated pyroclastic flows were apparent from a zone of vegetation that was charred on up-flow facing stems and extended ~ 75 m upwards from the valley floor. Third, flow-derived material had filled the valley to a depth of ~ 30 m by January 2001, forming a flat-topped deposit surfaced with mud that had ponded against the block flow (Figs. 3, 6 and 7).

Along the medial-to-distal section of the flow field, width had also increased dramatically since January 2001, to attain a maximum width of 495 m (Fig. 5; Table 1). This increase may be explained by filling and overtopping of the Nima II canyon. Filling of the valley by the flow meant that the flow width was no longer controlled by the dimensions of the ravine down which it extended.

Part of this width increase was the result of the emplacement of three short, stubby lobes along the western margin of the medial section (Fig. 6). These lobes comprised a ~ 780-m length of the western flow field margin, were 30–120 m thick, and extended ~ 130–170 m from the main stream in a southwesterly direction (Fig. 3). By January 2002 these lobes were inactive, isolated from the main southward moving stream by a prominent shear zone (Fig. 6). This dominant stream direction continued to follow the trend of the Nima II canyon, indicating that the main axis of advance remained controlled by the underlying topography.

The proximal section of the flow field also increased in thickness and width between January 2000 and 2002. This section is difficult to resolve in ETM+ band 8 and out-of-range for our laser range finders. Our analysis thus relies on year-on-year photographic comparison. On the flank of the Caliente dome, increased flow field thickness and width are apparent from a steady decrease in slope of the flow surface and burial of surrounding features, respectively (Fig. 8). The increase in width of the proximal flow field appears mostly to be the result of an increase in the width of the marginal levees, where the main stream has remained at a relatively constant width of ~ 75 m (Fig. 8).

4. Channel: morphology and dimensions

The flow field clearly displays the same systematic, spatial variations in structure and morphology as described by Lipman and Banks (1987) for the basaltic ′a′a flows emplaced during the 1984 eruption of Mauna Loa (Hawai′i). Using the classification and terminology of Lipman and Banks (1987) this can be summarized as four zones. These are, from toe to vent: flow toe, dispersed flowage, transitional channel, and stable channel.

4.1. Flow toe

Using field-based observations obtained during January 2000, Harris et al. (2002) detailed the structure, morphology, velocity profile and motion at the flow toe. These observations revealed that the surface crust was rubbley rather than blocky, consisting of 1–3 m wide rounded to sub-angular blocks, and the flow advanced in a caterpillar-track-like fashion resulting from a plug flow velocity profile. Where the core was exposed at an over-steepened frontal section, this was composed of massive, roughly oval (pillow-lava-like) lobes (Harris et al., 2002). The flow front in January 2002 was behaving in an identical manner, with a plug flow velocity profile causing debris to tumble from the flow top to gather in a talus zone at the flow base and to generate frequent ash plumes (Fig. 6). Larger ash plumes rose 50–300 m, where 61 such plumes were observed from a distance of ~ 4 km over a 6.5-h period on January 10, 2002 (Greg Bluth, January 2002 field notes).

4.2. Zone of dispersed flow

Across this zone, movement is dispersed across most of the flow width, a central channel and marginal shear zones being absent (Fig. 10). Across this zone, channel width therefore equals flow width. During January 2002, this zone extended 730 m back from the flow front and comprised a 210–375 m wide flow, with relatively low (29–73 m high) levees (Fig. 11). Fig. 11 also indicates that the

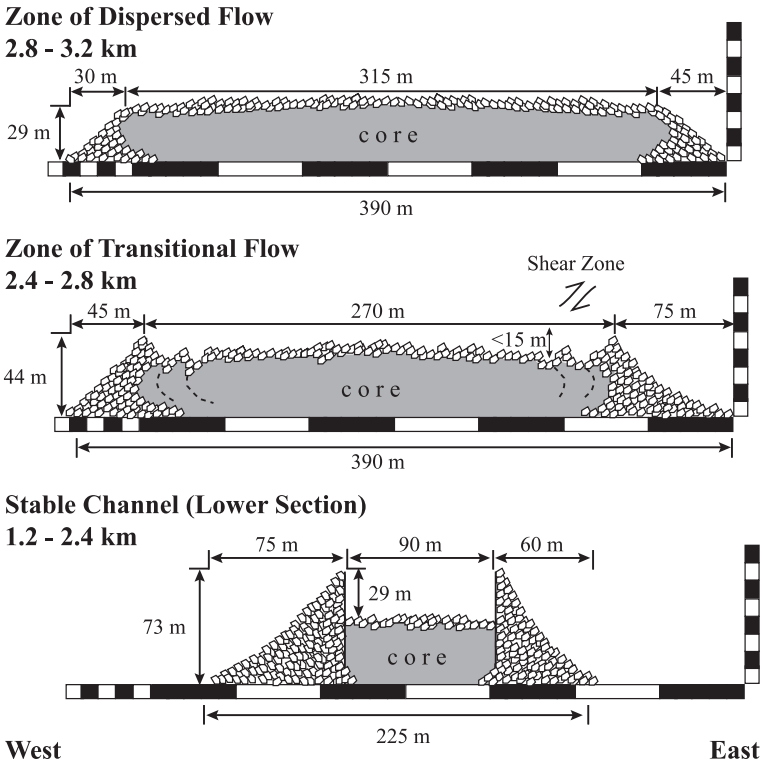

Fig. 10. Profiles typical of the zones of dispersed, transitional and stable channel flow. Profile dimensions are based on ETM+ January 2002 flow profile measurements take at down flow distances of 3225, 2880 and 1740 m, respectively.

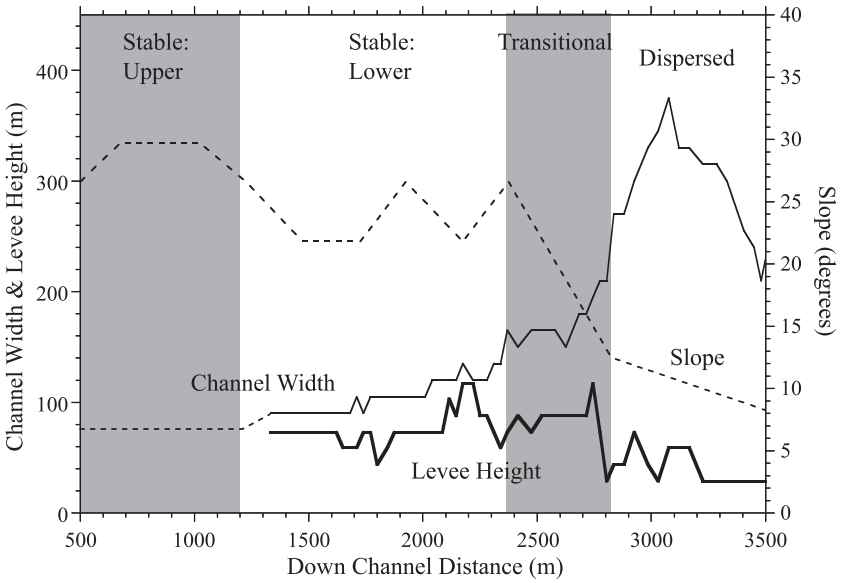

Fig. 11. Slope with ETM+ derived channel width and outer levee height. Each flow zone is located.

beginning of this zone occurs at a marked break in slope.

4.3. Transitional channel zone

This is a zone of transition between dispersed and channelized flow, and is marked by flow concentrated in a distinct central stream, bounded by shear zones that separate the stream from the static margins (Fig. 6). In agreement with Lipman and Banks (1987) the boundary between the transition zone and zone of dispersed flow is marked by a change in the shape of the profile from convex near the toe to a broad m-shaped profile up flow (Fig. 10). In January 2002, this zone was ~ 430 m long and comprised 165–180 m wide stream (Fig. 11), within a 300–380 m wide flow. The surface of the central stream was composed of a series of pressure ridges. We counted 15–16 over this channel length, giving a mean wavelength of 23–29 m. Pressure ridges were absent in the static marginal lobes that flank this zone (Fig. 6).

4.4. Stable channel zone

Within this zone the channel is extremely stable and well-defined, being bounded by well-developed levees (Fig. 6). Across this zone the channel and levees comprise the entire flow width (Fig. 3). Outer levee flanks lie at an angle of ~ 45° and consist of rubble buttressed by massive intrusions. The inner levee walls are near vertical and lined with a massive coating of lava. The flow surface is typically well below the levee crest and, as in the transitional zone, consists of a rubbley surface with pressure ridges. At Santiaguito, this zone can be split into two subsections: lower and upper.

As of January 2002, the lower section was ~ 1140 long, and extended from approximately the base of the Caliente dome to the beginning of the transitional zone. Along this section the channel width was 90–135 m, showed a steady increase in width down section and was contained within 44–117 m high levees (Fig. 11). A feature that distinguished this section from the transitional zone is that the surface of the lava flowing within the channel is significantly lower than the levee crest, being 29–59 m below the levee top as opposed to 0–15 m in the transitional zone (Fig. 10).

As of January 2002, the upper section extended ~ 1230 m from the vent to the base of the Caliente dome. The morphology of this section is similar to that of the transitional zone, in that flow entirely fills the channel and the channel–levee contact is marked by a line of shear (Fig. 4c). This zone, however, has been extremely stable and has changed little in morphology or width since January 1999, the main stream remaining ~ 75 m wide (Fig. 8).

4.5. Channel evolution

As of January 2000 the flow field lacked the stable channel zone. Instead, the flow comprised of an upper transitional zone that, although displaying well-formed outer levees and marginal shear zones (Fig. 4), lacked the morphology of the mature, stable channel (lower) zone. This upper section fed a zone of dispersed flow that comprised the two axes of advance mapped in Fig. 1a.

By January 2001, the medial section comprised a ~ 1-km-long section of well-formed channel that characterizes the lower section of the stable channel zone (Fig. 1b). This section formed on slopes of 22–27°, and began at the break of slope that marks the base of the Caliente dome. Above this, on slopes of 27–30°, the channel maintained the characteristics of the upper stable channel zone.

By January 2002, along the stable channel, the lower section had increased in length by ~ 800 m at the expense of the upper section. As in January 2001, the transition between these two sections occurred roughly at the break in slope, a point which has moved up slope due to filling of the topography at the dome base by the flow (Fig. 8).

5. Velocity, rheology, extrusion rates and volume

Flow front velocity obtained from the change in flow front positions recorded from the ground and/or ETM+ images are given in Table 2. These give a typical advance rate of 2–13 m day^{-1}. Such slow forward motion suggests a high viscosity (η), where η can be calculated using Jeffrey's equation:

$$\eta = (g\rho \sin\theta d^2)/(3V) \quad (2)$$

Table 2
Flow length, velocity and rheology

Date	Length (km)	Mean velocity (m day^{-1})	Mean levee width (m)	Slope (deg)	Viscosity ($\times 10^9$ Pa s)	Yield strength ($\times 10^5$ Pa)	Source
23-Jan-00	2.25	12	41	25	11–24	3.7	ETM+
31-Aug-00	2.65	2	–	11	31–69	–	field
30-Sep-00	3.05	13	–	11	4–9	–	field
31-Oct-00	3.35	10	–	11	6–13	–	field
30-Nov-00	3.55	7	–	11	8–19	–	field
31-Dec-00	3.65	3	–	11	17–39	–	field
25-Jan-01	3.75	4	36	11	14–32	0.7	ETM+
19-Jan-02	3.75	–	68	11	–	1.3	ETM+

in which g, ρ, θ, d and V are acceleration due to gravity, lava density (2600 kg m^{-3}), underlying slope, flow thickness and velocity, respectively. In Table 2, we calculate whole flow viscosities of 10^9–10^{10} Pa s using a flow thickness equal to the typical flow front height (20–30 m). We also calculate yield strengths (σ_o) of 10^4–10^5 Pa (Table 2) using levee width (w_L) in:

$$\sigma_o = g\rho\sin^2(\theta)2w_L \quad (3)$$

Our values for viscosity and yield strength are bulk or whole flow values, an integrated value that is the product of the rheological properties of both the flow core and crust. We have applied Jeffrey's equation, for example, to the flow as a whole recognizing that in reality the flow is comprised of liquid, solid and gas. In this regard, our viscosity estimate is an average for the entire flow and in reality deeper, higher temperature flow sections will be of a lower viscosity than cooler, near-surface sections (e.g. Stevenson et al., 2001). In addition, we have measured viscosity at only a single strain rate and therefore do not know the true shape of the shear stress–strain rate relationship; our viscosity results are thus, by definition, apparent viscosities (e.g. Shaw, 1969).

Extrusion rates calculated using the approach given in Appendix A indicate that extrusion rates have generally increased during 2000–2002, with a particularly large increase from 0.66 to 1.61 m^3 s^{-1} between January 2001 and January 2002 (Table 3). This increase is supported by the increase in volume during the two dates, which is also consistent with an increase in extrusion rates by a factor of ~ 2 (Table 3). Dimensionally, although this increase in extrusion rate has not yet resulted in an increase in flow length, it has been matched by an increase in flow area and thickness (Table 3).

6. Flow insulation and cooling rates

A feature of the Santiaguito block lava flow is that its surfaces are extremely cool and lack any incandescent cracks (Table 4). During our nighttime observations of 2000–2002 no incandesence was observed at any location except for in the vicinity of the vent. This results from the extremely slow emplacement velocities and lack of surface thermal renewal at this flow: velocities of 10 m day^{-1} mean that surfaces even within a few 10's of meters of the vent will have had days to cool. As described by Harris et al. (2002), this makes active block lava flows extremely hard to distinguish from the ambient background in ETM+ imagery, with no thermal anomaly apparent in bands 5 or 7 except at the vent and flow toe (Fig. 2).

Table 3
ETM+ derived flow area, effective radiation temperature (T_{surf}), volume and effusion rates (E_r)

Date	Active flow area (km^2)	Total flow field area (km^2)	T_{surf} (Eq. (A6)) (°C)	Volume ($\times 10^6$ m^3)	Mean thickness (m)	E_r (Eq. (A12)) (m^3 s^{-1})	dV/dt (m^3 s^{-1})
23-Jan-00	0.09–0.13	0.29	118–161	9.2	31	0.48	0.55
25-Jan-01	0.07–0.09	0.74	185–206	27.8	37	0.66	0.59
19-Jan-02	0.49–0.59	1.01	92–101	65.9	65	1.61	1.23

Table 4
ETM+ derived thermal characteristics

Date	January 23, 2000	January 25, 2001	January 19, 2002
Crust temperature			
Minimum (°C)	53	34	31
Maximum (°C)	86	86	86
Mean (°C)	68	50	49
Standard deviation (°C)	12	16	16
Radiative heat loss			
Minimum (W m^{-2})	635	501	481
Maximum (W m^{-2})	934	934	934
Mean (W m^{-2})	764	620	609
Standard deviation (W m^{-2})	106	136	130
Convecttive heat loss			
Minimum (W m^{-2})	77	8	2
Maximum (W m^{-2})	252	252	252
Mean (W m^{-2})	152	71	65
Standard deviation (W m^{-2})	62	78	73
Thermal boundary layer thickness			
Minimum (m)	1.9	1.9	1.9
Maximum (m)	3.4	4.8	5.1
Mean (m)	2.6	3.7	3.8
Standard deviation (m)	0.5	0.9	0.9
Core cooling per meter			
Minimum (°C m^{-1})	0.057–0.095	0.041–0.068	0.039–0.064
Maximum (°C m^{-1})	0.095–0.158	0.095–0.158	0.095–0.158
Mean (°C m^{-1})	0.074–0.122	0.056–0.092	0.054–0.090
Standard Deviation (°C m^{-1})	0.014–0.022	0.017–0.029	0.016–0.027
Core cooling per hour			
Minimum (°C h^{-1})	0.027–0.055	0.019–0.039	0.018–0.037
Maximum (°C h^{-1})	0.045–0.091	0.045–0.091	0.045–0.091
Mean (°C h^{-1})	0.035–0.070	0.026–0.053	0.025–0.052
Standard deviation (°C h^{-1})	0.006–0.013	0.008–0.016	0.008–0.016
Cooling-limited length[a]			
Maximum (km)	3.5–2.1	4.9–2.9	5.1–3.1
Minimum (km)	2.1–1.3	2.1–1.3	2.1–1.3
Mean (km)	2.7–1.6	3.6–2.2	3.7–2.2
Cooling-limited duration[a]			
Maximum (days)	311–152	434–213	458–225
Minimum (days)	186–91	186–91	186–91
Mean (days)	241–118	320–157	328–161

[a] Assumes that the slow stops flowing when the core has cooled by 200 °C.

Satellite, ground and helicopter-based thermal measurements are in good agreement and show that, after the first ~500 m, surface temperatures are less than 75 °C and typically ~40 °C (Fig. 12). This is only a little warmer than adjacent ambient surfaces where, during helicopter-based measurements in January 2002, a mean surface temperature of 38 ± 8 °C for the medial flow section compared

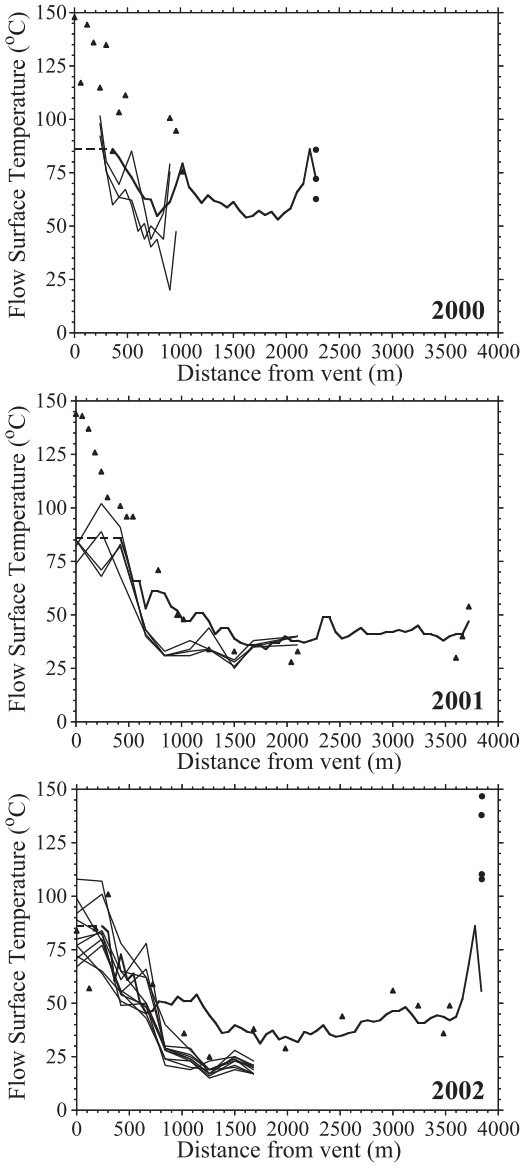

Fig. 12. Down-flow surface temperature profiles obtained from ETM+(thick black line), ground-based radiometers (thin black line), and helicopter-based radiometers (triangles). Flow front temperatures (circles) were obtained from the ground in 2000 and from helicopter in 2002. Saturated ETM+ values (i.e. $T_{surf} \geq 86$ °C) are given by the broken line.

with 29 ± 2 °C obtained from the surrounding jungle. The outer levees are even cooler, where we obtained 31 ± 4 °C (range: 23–47 °C) for the outer levee from field site B (Fig. 1a) during January 2002. The low values obtained from our ground-based profiles between 750 and 2000 m during 2001 and 2002 thus result from these being levee rather than flow surface temperatures.

In all cases, the thermal profiles show the same down flow variation as described by Harris et al. (2002) for the 2000 case. Highest temperatures are typically found proximally, where the crust is still relatively recent. Away from the vent, however, temperatures decrease rapidly to a low, constant value across the medial section (Fig. 12). At the flow toe, a peak is apparent due to exposure of hotter material during to frequent avalanches of crust down the flow front.

An extremely thick, cool and stable surface crust makes block flows an extremely well insulated form of lava flow emplacement: heat loss is extremely low resulting in slow cooling of the core (Table 4). Low cooling rates mean that block flows are capable of extending a surprising distance in spite of extremely slow advance rates and low eruption rates. In this case, insulation means that the flow core will take 3–15 months to cool by 200 °C, by which time (moving at a typical velocity of 12.5 ± 1.3 m day^{-1}), the flow will have extended 2–5 km (Table 4).

7. Conclusions

Effusive eruptions of silicic lava are usually associated with the emplacement of lava domes or, if the lava rheology and/or ground slope are appropriate, coulees or block lava flows (Blake, 1990). Block lava flows are therefore typically silicic flows that Macdonald (1953) described as having a surface composed of smooth polyhedral blocks. Although the current lava flow at Santiaguito is silicic (~ 62.5 wt.% SiO_2), the surface is not blocky. Instead the surface is composed of decimeter to meter scale, rounded-to-sub-angular rubble. This may be a result of relatively high extrusion rates or slow cooling (Anderson et al., 1998), or the relatively low silica content of this flow when compared with other truly blocky dacitic and rhyolitic lava flows. We note, however, that the viscosity for the Santiaguito flow does appear to be similar to that calculated for dacitic and rhyolitic flows (Table 5). Thus the failure to form blocks may not be a function of viscosity. Here, we

Table 5
Viscosity and silica content for other silicic lava flows

Viscosity (Pa s)	Location	Silica content (wt.%)	Method	Reference
10^5–10^7 (900–1000 °C)	Mount Hood Andesite, Oregon, USA	60–61	lab-based[a]	Murase and McBirney (1973)
4.6×10^9	Chao Dacite Flow, N. Chile	67–69[b]	surface folds[c]	Fink (1980)
10^9–10^{10}	Colima Andesite Mexico	59	Eq. (2)	Navarro-Ochoa et al. (2002)
3.5×10^9–1.2×10^{10}	Badlands Rhyolite Flow, Idaho, USA	75–77	lab-based[d]	Manley (1996)
4×10^9–6.9×10^{10}	Santiaguito Dacite Flow, Guatemala	62.5	Eq. (2)	This Study
7.5×10^{10}–5.2×10^{11}	Karisimbi Trachyte, Rwanda	61	surface folds[c]	McKay et al. (1998)
10^7–10^{13} (1000–600 °C)	Newberry Rhyolite, Oregon, USA	72–74	lab-based[a]	Murase and McBirney (1973)

[a] Methodology of Murase and McBirney (1973).
[b] From de Silva et al. (1994).
[c] Methodology of Fink (1980).
[d] Methodology of Shaw (1972).

apply the term block flow to distinguish this silicic flow from basaltic pahoehoe or 'a'a. In the observed case, over three years, the block flow has developed a spatial structure identical to that observed during basaltic eruptions (Lipman and Banks, 1987), where a well-defined and stable master channel feeds a distal zone of dispersed flow.

Our measurements and observations of the evolution of this flow field allow us to define 3 key characteristics of block flow emplacement.

(1) Advance rates are extremely slow (maximum of tens of meters per day), implying relatively high whole flow viscosities of 10^9–10^{10} Pa s. This compares well with viscosities of 10^8–10^{12} Pa s obtained for other silicic flows (Table 5).

(2) The extremely high and wide (up to 117 m high and 120 m wide) levees imply high yield strengths, where we calculate 10^4–10^5 Pa. This compares well with yield strengths of 10^4–10^5 Pa calculated for other silicic flows (Blake, 1990; McKay et al., 1998; Lyman, 2001). This results in a high aspect ratio (height/width) which in January 2002 was 4–7.

(3) In agreement with the modeling of Manley (1992), thick and cool surface crusts provide extremely effective thermal insulation. In our case this has allowed the block flow to advance 3.75 km in spite of extremely low extrusion rates (0.5–1.6 m^3 s^{-1}) and velocities (1.1–4.7 km $year^{-1}$). In short, low rates of core cooling ($\sim$ 0.05 °C h^{-1}) allows the flow to remain capable of forward motion for many months.

In terms of Santiaguito, the current flow front has remained at 3.75 km from the vent for $\sim$ 12 months. Given the results of our calculations in Table 4, this may be a result of the flow having attained its maximum cooling limited length. Within the limits of Eq. (A14), the only way for the flow to extend any further would be by an increase in flow thickness or forward velocity, both of which may result from an increase in extrusion rate.

Interestingly, the eruption rate appears to have increased during 2001 from $\sim$ 0.6 m^3 s^{-1} during 2000–2001 to $\sim$ 1.4 m^3 s^{-1} by 2002. This latter value is extremely high for Sanatiaguito, where such extrusion rates have not been witnessed since 1963. Alternatively, the time averaged estimates that have been made to date may have missed such high effusion rate spurts. We note, however, the highest extrusion rate measured during frequent satellite-based measurements between 1987 and 2001 has been 0.95 m^3 s^{-1} (Harris et al., 2003). This value was obtained during the high extrusion rate phase of 1986–1989 when a 3.6-km-long block lava flow was emplaced (Fig. 1a). Thus such high extrusion rate spurts must either be of short (<1 year) duration or Santiaguito is currently reversing an 80-year-long trend of declining extrusion rates (Harris et al., 2003).

As mentioned in the introduction, in presenting our analysis we have attempted to illustrate how ETM+ data can be used to track, measure and map an evolving silicic lava flow field. In this regard, a major asset of the ETM+ flown on Landsat 7 over that of its predecessor, the Thematic Mapper (TM) flown on Landsats 4 and 5, is the improved spatial resolution of the thermal infrared band (Fig. 2). This

has been improved from 120 to 60 m. In the case of Santiaguito, this is particularly useful given that there are no short-wave infrared thermal anomalies along most of the lava flow due to coverage of an extensive and cool surface crust. The new 15-m panchromatic band of ETM+ is also extremely valuable in allowing measurements of levee heights, flow dimensions and, therefore, flow volumes. However, it is unfortunate that future Landsat-class satellites will not have the thermal band that allows us to monitor active domes and silicic lava flows such as that at Santiaguito.

A number of operational characteristics also make the ETM+ useful for volcano studies. Here, ETM+ has a more favorable duty cycle than the Advanced Spaceborne Thermal Emission and Reflection Radiometer (ASTER), allowing ETM+ to collect images for longer periods of time than the latter instrument. ETM+ data are also processed promptly at the Earth Resources Observation Systems (EROS) data center (EDC) with images being shipped by FTP within 3 days of collection. In addition, the ETM+ cloud detection algorithm and online quick-look capabilities combine to make it easy to assess the quality of data with respect to the volcanogical application that the data will be used for. To utilize these capabilities, the Landsat 7 Science Team has established a list of volcano targets that are regularly acquired ensuring updated ETM+ images for most of the world's active volcanoes.

Acknowledgements

Much of this work was funded by NASA grant NAG5-9413. Jon Dehn, Mike Ramsey and Scott Rowland provided many helpful comments that improved the final version of this manuscript.

Appendix A

The following methodologies are summarized from Harris et al. (2002, 2003) and references therein. For definition of terms see Table A1. For further details and parameter values see Harris et al. (2003).

Table A1
Definition of terms used in Eqs. (A1)–(A14)

Parameter	Definition
α	Air cubic expansivity
A_{lava}	Lava flow area
A_{pixel}	band 6 pixel area
A_6	thermal anomaly area in band 6
c_{L}	latent heat of crystallization
C_{p}	lava specific heat capacity
d	flow depth
$\Delta\phi$	post-eruption crystallization
ΔT	lava cooling
$\delta T/\delta x$	down-flow core cooling rate
ε_λ	surface emissivity at wavelength λ
E_r	lava volumetric extrusion rate
f	portion of flow surface occupied by hot cracks
h_{base}	basal crust thickness
h_{surf}	surface crust thickness
G	acceleration due to gravity
k	air thermal conductivity
κ	air thermal diffusivity
k_{lava}	lava thermal conductivity
$L(\lambda,T)$	Planck's function for a blackbody emitting at wavelength λ and temperature T
λ	central wavelength of band x
μ	air dynamic viscosity
n_x	number of thermally anomalous pixels in band x
p	anomaly portion occupied by hot cracks at temperature T_{h}
p_b	anomaly portion occupied by ambient background at temperature T_{b}
pixel_x	pixel area in band x
Q_{base}	heat lost by conduction from the flow base
Q_{cond}	heat conducted through the surface crust
Q_{conv}	convective heat loss
Q_{pixel}	total heat loss from a pixel
Q_{rad}	radiative heat loss
Q_{tot}	total heat loss from the lava flow
ρ	air density
ρ_{lava}	lava density
$R_{\text{R}\lambda}$	reflected radiation at wavelength λ
$R_{\text{U}\lambda}$	radiation upwelling from the atmosphere at wavelength λ
R_{xint}	integrated radiance in band x
σ	Stefan Boltzmann constant
T_{air}	air temperature
T_{b}	temperature of ambient (background) surfaces
T_{base}	temperature at flow base
T_{c}	crust temperature on active lava flow
T_{core}	lava flow core temperature
T_{h}	hot crack temperature
R_{xi}	emitted radiance in band x for pixel i
T_{sat}	satellite-recorded temperature
T_{surf}	lava flow surface effective radiation temperature
τ_λ	atmospheric transmissivity at wavelength λ
V	lava flow velocity

Following Harris et al. (2003), block lava flow thermal structure can be obtained from solution of:

$$R_{5\text{int}} = p_b L_5(T_b) + pL_5(T_h) + (1 - p_b - p)L_5(T_c) \quad \text{(A1)}$$

$$R_{6\text{int}} = p_b L_6(T_b) + pL_6(T_h) + (1 - p_b - p)L_6(T_c) \quad \text{(A2)}$$

$$R_{7\text{int}} = p_b L_7(T_b) + pL_7(T_h) + (1 - p_b - p)L_7(T_c) \quad \text{(A3)}$$

in which $R_{x\text{int}}$ is the band x radiance integrated over the entire band 6 thermal anomaly:

$$R_{x\text{int}} = \sum_{i=1}^{nx} \left(\frac{\text{pixel}_x}{A_6} R_{xi} \right) \quad \text{(A4)}$$

Now the lava flow area (A_{lava}) can be calculated from:

$$A_{\text{lava}} = pA_6 + (1 - p_b - p)A_6 \quad \text{(A5)}$$

and the effective radiation temperature of the flow surface (T_{surf}) from:

$$T_{\text{surf}} = [fT_h^4 + (1 - f)T_c^4]^{0.25} \quad \text{(A6)}$$

in which $f = p/[p + (1 - p_b - p)]$. This allows calculation of the radiative and convective heat losses from the flow surface:

$$Q_{\text{rad}} = \sigma \varepsilon A_{\text{lava}} T_{\text{surf}}^4 \quad \text{(A7)}$$

$$Q_{\text{conv}} = 0.14 A_{\text{lava}} k (g \ \alpha \ \rho/\mu\kappa)^{1/3} (T_{\text{surf}} - T_{\text{air}})^{4/3} \quad \text{(A8)}$$

Assuming that all heat conducted across the flow crust (Q_{cond}) is lost from the surface by Q_{rad} and Q_{conv} (i.e. $Q_{\text{cond}} = Q_{\text{rad}} + Q_{\text{conv}}$), the surface crust thickness (h_{surf}) can be calculated from:

$$h_{\text{surf}} = k_{\text{lava}} (T_{\text{core}} - T_{\text{surf}})/Q_{\text{cond}} \quad \text{(A9)}$$

Heat loss through the flow base (Q_{base}) can be obtained from

$$Q_{\text{base}} = A_{\text{lava}} k_{\text{lava}} [(T_{\text{core}} - T_{\text{base}})/h_{\text{base}}] \quad \text{(A10)}$$

and total flow heat loss (Q_{tot}) from:

$$Q_{\text{tot}} = Q_{\text{rad}} + Q_{\text{conv}} + Q_{\text{base}} \quad \text{(A11)}$$

Now extrusion rate (E_r) can be calculated from

$$E_r = Q_{\text{tot}}/[\rho_{\text{lava}} (C_p \ \Delta T + c_L \ \Delta \phi)] \quad \text{(A12)}$$

As found by Harris et al. (2002), most of the Santiaguito block flow the surface is extremely cool (≤ 111 °C) and isothermal (lacking in cracks: 100% crust coverage). For pixels where a cool, isothermal surface exists, T_{surf} can be approximated from the brightness temperature in band 6, where:

$$L(\lambda, T_{\text{surf}}) = \tau_\lambda [\varepsilon_\lambda L(\lambda, \ T_6) + R_{R\lambda}] + R_{U\lambda} \quad \text{(A13)}$$

This approach is used to obtain down-flow thermal profiles where, to ensure that a pixel is entirely filled with lava, we only use pixels falling along the flow center line. In this case, substituting A_{lava} with A_{pixel} in Eqs. (A7) and (A8) and summing Q_{rad} and Q_{conv} allows us to calculate total heat loss from each pixel (Q_{pixel}). Assuming that heat produced by latent heat of crystallization and lost through the base of the flow per unit length is negligible, we calculate down-flow core cooling ($\delta T/\delta x$) using Q_{pixel} in:

$$\delta T/\delta x = (Q_{\text{pixel}}/A_{\text{pixel}})/(dV \rho_{\text{lava}} C_p) \quad \text{(A14)}$$

References

Anderson, S.W., Stofan, E.R., Plaut, J.J., Crown, D.A., 1998. Block size distributions on silicic lava flow surfaces: implications for emplacement conditions. Geol. Soc. Am. Bull. 110 (10), 1258–1267.

Blake, S., 1990. Viscoplastic models of lava domes. In: Fink, J.H.Lava Flows and Domes. Springer-Verlag, Berlin, pp. 88–126.

de Silva, S.L., Self, S., Francis, P.W., Drake, R.E., Carlos Ramirez, R., 1994. Effusive silicic volcanism in the Central Andes: the Chao dacite and other young lavas of the Altiplano–Puna Volcanic Complex. J. Geophys. Res. 99 (B9), 17805–17825.

Fink, J., 1980. Surface folding and viscosity of rhyolite flows. Geology 8, 250–254.

Flynn, L.P., Harris, A.J.L., Wright, R., 2001. Improved identification of volcanic features using Landsat 7 ETM+. Remote Sens. Environ. 78, 180–193.

Harris, A.J.L., Flynn, L.P., Matías, O., Rose, W.I., 2002. The thermal stealth flows of Santiaguito: implications for the cooling and emplacement of dacitic block lava flows. Geol. Soc. Am. Bull. 114 (5), 533–546.

Harris, A.J.L., Flynn, L.P., Rose, W.I., 2003. Temporal trends in Lava Dome Extrusion at Santiaguito 1922–2000. Bull. Volcanol 65, 77–89.

Lipman, P.W., Banks, N.G., 1987. Aa flow dynamics, Mauna Loa 1984. U.S. Geol. Surv. Prof. Pap. 1350, 1527–1567.

Lyman, A., 2001. The effects of slope on the growth and collapse of lava domes. M.S. thesis, Arizona State Univ., 115 pp.

Macdonald, G.A., 1953. Pahoehoe, aa, and block lava. Am. J. Sci. 251, 169–191.

Manley, C.R., 1992. Extended cooling and viscous flow of large, hot rhyolite lavas: implications of numerical modeling results. J. Volcanol. Geotherm. Res. 53, 27–46.

Manley, C.R., 1996. Physical volcanology of a voluminous rhyolite lava flow: the Badlands lava, Owyhee Plateau, southwestern Idaho. J. Volcanol. Geotherm. Res. 71, 129–153.

McKay, M.E., Rowland, S.K., Mouginis-Mark, P.J., Garbeil, H., 1998. Thick lava flows of Karisimbi Volcano, Rwanda: insights from SIR-C interferometric topography. Bull. Volcanol. 60, 239–251.

Murase, T., McBirney, A., 1973. Properties of some common igneous rocks and their melts at high temperatures. Geol. Soc. Am. Bull. 84, 3563–3592.

Navarro-Ochoa, C., Gavilanes-Ruiz, J.C., Cortes-Cortes, A., 2002. Movement and emplacement of lava flows at Volcan de Colima, Mexico: November 1998–February 1999. J. Volcanol. Geotherm. Res. 117, 155–167.

Rose, W.I., 1972. Pattern and mechanism of volcanic activity at the Santiaguito volcanic dome, Guatemala. Bull. Volcanol. 36, 73–94.

Rose, W.I., 1987. Volcanic activity at Santiaguito Volcano, 1976–1984. Spec. Pap. Geol. Soc. Am. 212, 17–28.

Shaw, H., 1969. Rheology of basalt in the melting range. J. Petrol. 10 (3), 510–535.

Shaw, H., 1972. Viscosities of magmatic silicate liquids: an empirical method of prediction. Am. J., 870–893.

Stevenson, R.J., Dingwell, D.B., Bagdassarov, N.S., Manley, C.R., 2001. Measurement and implication of "effective" viscosity for rhyolite flow emplacement. Bull. Volcanol. 63, 227–237.